Journal of Applied Analysis and Computation
Volume 16, Number 1, February 2026, 426–457
Website:http://www.jaac-online.com
DOI:10.11948/20250153

JOINT COMPUTATIONAL STUDY OF GLOBAL STABILITY AND PARAMETER ESTIMATION IN SEIR MODELS USING A PHYSICS-INFORMED NEURAL NETWORK

Shahbaz Ahmad[1,†], Gunesh Kumar[1] and Manuel De la Sen[2]

Abstract This study presents a Physics-Informed Neural Network (PINN) framework for simulating disease dynamics governed by the Susceptible-Exposed-Infectious-Recovered (SEIR) model. Utilizing a fully connected neural network implemented in PyTorch, the approach employs automatic differentiation to enforce initial conditions and solve the system of ordinary differential equations (ODEs) associated with the SEIR model. The PINN is trained using a composite loss function that integrates boundary conditions with physics-based constraints, allowing for accurate modeling of the temporal evolution of all SEIR compartments. Beyond forward simulation, this work addresses the inverse problem of parameter estimation specifically, identifying the time-dependent contact rate using temporal epidemiological data. By training the network on observed data for the susceptible, exposed, infectious, and recovered populations, the model approximates the solution vector and simultaneously minimizes a loss that combines data fidelity with the residual of the SEIR system. A key contribution of this study is the numerical demonstration of the SEIR system's global stability without assuming a constant population size, achieved via a generalized Lyapunov theorem. Additionally, physical constraints embedded directly into the learning process enhance the model's ability to inform control strategies and ensure long-term system stabilization. This machine learning-based framework offers a robust and flexible tool for both understanding disease spread and conducting real-time epidemiological inference. It highlights the potential of PINNs for solving complex inverse problems, improving predictive accuracy, and supporting data-driven decision-making in public health. The code can be downloaded from https://github.com/shahbaz1982/SEIR.

Keywords SEIR model, non linear dynamics, epidemic modeling, global stability, physics-informed neural networks.

MSC(2010) 92D30, 34D23, 68T07.

1. Introduction

Mathematical modeling plays a crucial role in epidemiology by identifying the most effective strategies for disease prevention and control, while also offering insights into the underlying factors that influence disease transmission. In 1766, Daniel Bernoulli made the first known application of mathematical modeling to the study of infectious disease spread [12]. In his

[†]The corresponding author.
[1]ASSMS, Government College University, Lahore, Pakistan
[2]Automatic Control Group–ACG, Institute of Research and Development of Processes, Department of Electricity and Electronics, Faculty of Science and Technology, University of the Basque Country (UPV/EHU), 48940 Leioa, Spain
Email: shahbazahmad@sms.edu.pk(S. Ahmed), gunesh.kumar_22@sms.edu.pk(G. Kumar), manuel.delasen@ehu.eus(M. De la Sen)

study, which is still highly significant today, he created and resolved a differential equation that described the dynamics of infection. In 1927, Kermack and McKendrick [21] presented the first fundamental compartmental model that clarifies the dynamics of infectious disease transmission. Their SIR model utilizes ordinary differential equations to track the numbers of susceptible, infected, and recovered individuals throughout an outbreak. In [4], Anderson et al. presented standard mathematical models for infectious disease transmission, which have been valuable in studying various diseases worldwide. The progress of mathematical epidemiology was slow due to a limited understanding of infection spread until the early 20th century.

Most conventional compartmental models are derived from Kermack and McKendrick's original SIR model [21], which categorizes the population into three classes: susceptible (S), infected (I), and recovered (R) individuals. For certain diseases, such as influenza and tuberculosis, a susceptible individual can be exposed for a period after coming into close contact with an infectious person; during this time, they may become ill but are not yet contagious. In order to create a Susceptible-Exposed-Infectious-Recovered (SEIR) model, it makes sense to add an exposed (E) compartment. The SEIR model is one of the most important compartmental models of epidemics [20]. It is very popular and widely used in different contexts [8, 33, 34, 36, 37, 51]. The evolution of the relative proportions of four types of individuals within a particular population is described by this model. Specifically, susceptible individuals (S) can contract the disease and transmit it to others; asymptomatic individuals (E) and symptomatic individuals (I) are contagious and can spread the disease to susceptible individuals. In contrast, recovered individuals (R) acquire lifelong immunity after recovery or, in some cases, death. Generally speaking, SEIR models incorporate diseases with an incubation period and generalize SIR models. The SEIR model is widely studied in the literature [4, 5, 10, 11, 13, 17, 19, 28, 40] due to its theoretical and practical significance. Many significant results have been established on threshold values that determine whether an infectious disease will vanish, as well as on the local and global stability of disease-free and endemic equilibrium points [44, 50, 57]. Additionally, studies have analyzed equilibrium points to assess whether an epidemic will persist (endemic equilibrium) or die out (disease-free equilibrium) in the host population [2, 29, 54].

In the study conducted by [29], the global stability of the SEIR model was established using a general criterion for the orbital stability of periodic orbits related to higher-dimensional nonlinear autonomous systems, under the assumption of a constant population size. However, it's noteworthy that Li's demonstration relies on the conclusions of Hirsch, which were validated only for $n = 3$ and not extended to $n = 4$ (here, "n" refers to the dimension of the system of differential equations describing the SEIR model). This limitation necessitates Li's assumption of a constant population size. Furthermore, in the works of [24–26, 30] and [35], the authors also assumed a constant population size, enabling them to simplify the system and focus solely on the reduced system described by the first three equations. Subsequently, they applied the LaSalle invariance principle to demonstrate the global stability of this reduced system. In our study, we extend the findings of [35] by numerically demonstrating the global stability of the SEIR system using Physics-Informed Neural Networks (PINNs), without assuming a constant population size. While Runge-Kutta (RK) solvers, as used in [35], are well-suited for deterministic, well-posed problems, PINNs offer significant advantages in scenarios involving real-world data, parameter inference, and generalization across different conditions. This makes PINNs particularly valuable for solving SEIR models in epidemiological research, where uncertainties and incomplete information are common.

Deep learning techniques for partial differential equation (PDE) solving have gained popu-

larity recently because of their ease of use, mesh-free methodology, and efficiency when dealing with inverse problems and high-dimensional spaces [32, 41, 43, 52]. The deep Ritz method [56], the deep Galerkin method [46], and physics-informed neural networks (PINNs) [42] are important methods in scientific machine learning. These methods use deep neural networks (DNNs) to minimize a loss function that takes into account domain-specific information and physical laws in order to approximate differential equation solutions [14, 15, 38]. In particular, the loss function integrates the differential equation residual, boundary and beginning conditions, and occasionally observational data in the case of PINNs [42], which are the subject of this work.

In this paper, specifically, we analyze the findings of [35] using PINNs and establish the global stability of the full SEIR system numerically, without imposing constraints on population size. This is accomplished by leveraging a generalized version of the Lyapunov theorem proposed by [7]. A key objective of this study is to develop a control law aimed at eradicating infection persistence within the host population. Recognizing the importance of control and stabilization in epidemiological models such as SEIR, various strategies have been proposed [3, 31, 35, 39, 49, 55]. Among these, PINNs have demonstrated effectiveness by incorporating physical constraints directly into the learning process. By employing a recursive Lyapunov-based approach, PINNs enhance global stability and tracking accuracy for systems with strict feedback [27], making them a powerful tool for solving complex differential equations. In addition to forward simulation, this work tackles the inverse problem of parameter estimation, focusing on identifying the time-varying contact rate from temporal epidemiological data. The neural network is trained on observed data from the susceptible, exposed, infectious, and recovered compartments, allowing it to approximate the system's solution while minimizing a loss function that balances data accuracy with the residuals of the SEIR model's governing equations. Additionally, we investigate the conditions required to ensure the positivity and boundedness of solutions [44, 45, 50, 57], as well as factors that may lead to oscillatory behavior in the system's dynamics [1, 2, 45]. Our research shows that solutions that begin with positive initial conditions stay positive after some fluctuation by taking advantage of the solutions ongoing dependence on the initial data. This insight is significant in real-world scenarios, as diseases often emerge with initially positive data rather than strictly positive values. Furthermore, our examination of the local stability of the SEIR model, numerically, deviates from previous approaches in the literature (see [9, 35, 53]).

The structure of this paper is organized as follows: We introduce the SEIR epidemic model in the next section. Section 3 examines the existence, boundedness, and positivity of solutions, evaluates the local stability of system (2.1). In Section 4, we outline the Physics-Informed Neural Networks (PINNs) approach for solving the SEIR model. Section 5 presents the results obtained with the PINNs and compares them with existing literature. Section 6 presents the information of parameter identification using PINNs. Finally, the last section discusses system synchronization and provides a brief summary.

2. The SEIR epidemic model

In this paper, we introduce the SEIR epidemic model governed by the following equations [1] to analyze and study the key objectives defined earlier:

$$\begin{aligned}\frac{dS}{dt} &= A - \mu S(t) - \beta S(t)I(t),\\ \frac{dE}{dt} &= \beta S(t)I(t) - (\sigma + \mu)E(t),\end{aligned}$$

$$\frac{dI}{dt} = \sigma E(t) - (\alpha + \mu + \gamma)I(t),$$
$$\frac{dR}{dt} = \gamma I(t) - \mu R(t), \tag{2.1}$$

subject to the initial conditions $S(0) \geq 0$, $E(0) \geq 0$, $I(0) \geq 0$, and $R(0) \geq 0$, the SEIR model is formulated as follows. In this model $S(t)$, $E(t)$, $I(t)$, and $R(t)$ represent the number of susceptible, exposed, infectious, and recovered individuals at time t, respectively. The parameters are defined as follows: A is the recruitment rate of new individuals into the susceptible class, σ is the rate at which exposed individuals become infectious, β is the average number of contacts per infectious individual per unit time, γ is the natural recovery rate of infectious individuals, μ is the natural mortality rate of the population and α is the disease-induced mortality rate. Note that $\frac{1}{\sigma}$ represents the average latency period.

3. Some properties of the SEIR epidemic model

In this section, we analyze the well-posedness of the solutions to (2.1), establishing their global existence, uniqueness, nonnegativity, and boundedness, though without providing detailed proofs. For a thorough examination of these properties, we refer the reader to [1,24–26,30,35]. For convenience, we define ($\mu_1 := \alpha + \mu$) for the subsequent discussions and throughout the remainder of this work.

3.1. Boundedness and positivity of the solutions

Theorem 3.1. *Let S_0, E_0, I_0, $R_0 \in R$ be given. (2.1) has a single non-extendable solution (S, E, I, R) that confirms that $(S, E, I, R)(0) = (S_0, E_0, I_0, R_0)$. This solution is defined on a maximal interval* [35].

Theorem 3.2. *For any given initial conditions $S_0 > 0$, $E_0 > 0$, $I_0 > 0$, $R_0 > 0$ pertaining to system (2.1), the non-extendable solution provided by Theorem 3.1 is global and remains positive for all $t \geq 0$* [35].

Theorem 3.3. *Let Ω be the set defined by*

$$\Omega = \left\{ (S, E, I, R) \in \mathbb{R}^4_+ \quad / \quad 0 \leq S + E + I + R \leq \frac{A}{\mu} \right\}.$$

As a result, Ω is positively invariant, ensuring that all solutions of (2.1) initiated in $\mathbb{R}^4_+$ are ultimately bounded and will eventually enter the attractive set Ω [35].

3.2. Local stability of the equilibria

Now, we investigate the model to compute the basic reproduction number, identify the conditions required for the existence of a non-trivial equilibrium, and assess the local and global asymptotic stability of the equilibrium points.

3.2.1. Basic reproductive number

In this subsection, we define the basic reproduction number R_0 for the system represented by (2.1). The basic reproduction number R_0 indicates the average number of secondary infections

caused by one infectious individual in a fully susceptible population [11, 13]. In various deterministic epidemiological models, an infection can take hold in a fully susceptible population only when $R_0 > 1$. Consequently, the basic reproduction number R_0 is frequently considered a threshold parameter that dictates whether an infection can invade and persist within a new host population.

A disease-free equilibrium $E_0 = (\frac{A}{\mu}, 0, 0, 0)$ is clearly present in the system described by (2.1). In this framework, the variables E and I denote the components related to infection. The transition matrix V and the new infection matrix F are defined as follows:

$$F = \begin{pmatrix} 0 & \beta\dfrac{A}{\mu} \\ 0 & 0 \end{pmatrix} \quad \text{and} \quad V = \begin{pmatrix} \sigma+\mu & 0 \\ -\sigma & \mu_1+\gamma \end{pmatrix}. \tag{3.1}$$

For the model represented by (2.1), the basic reproduction number is defined as the spectral radius of the next generation matrix (FV^{-1}) [18], which is expressed as follows:

$$R_0 := \rho(FV^{-1}) = \frac{\sigma\beta A}{\mu\ (\sigma+\mu)\ (\mu_1+\gamma)}, \tag{3.2}$$

which provides a quantification of the disease risk.

In addition, another endemic equilibrium point $E^* = (S^*, E^*, I^*, R^*)$ is present when $R_0 > 1$ in the system outlined by (2.1),

$$\begin{aligned} S^* &= \frac{A}{\mu R_0}, \\ E^* &= \frac{\mu\ (R_0-1)(\mu_1+\gamma)}{\sigma\beta}, \\ I^* &= \frac{\mu\ (R_0-1)}{\beta}, \\ R^* &= \frac{\gamma\ (R_0-1)}{\beta}. \end{aligned}$$

Within the context of linear ordinary differential equations (ODEs), it is generally acknowledged that the eigenvalues of the system exclusively dictate its stability properties. Nevertheless, given that our model (2.1) is nonlinear, it is necessary to implement linearization and apply a theorem from [16] to connect the local dynamics of the linear and nonlinear systems.

We will analyze the local stability characteristics of the equilibrium points by linearizing the nonlinear system represented by the differential equation (2.1) around the points E_0 and E^*. Next, we will apply small perturbations to the system at these equilibrium points and investigate the long-term behavior that follows. To achieve this, we linearize the system at each equilibrium point using the Jacobian matrix related to system (2.1). The Jacobian matrix of the system described by (2.1) at an arbitrary equilibrium point $E_* = (S_*, E_*, I_*, R_*)^T$ can be represented as follows:

$$J(E^*) = \begin{pmatrix} -\mu-\beta I_* & 0 & -\beta S_* & 0 \\ \beta I_* & -(\sigma+\mu) & \beta S_* & 0 \\ 0 & \sigma & -(\mu_1+\gamma) & 0 \\ 0 & 0 & \gamma & -\mu \end{pmatrix}. \tag{3.3}$$

Hence, the corresponding characteristic equation can be written as:

$$(\lambda+\mu)\ (\lambda^3+a\lambda^2+b\lambda+c)=0, \tag{3.4}$$

where

$$\begin{aligned}
a &= (\mu_1+\gamma)+(\sigma+\mu)+\mu+\beta I_*,\\
b &= -(-\mu-\beta I_*)\ ((\mu_1+\gamma)+(\sigma+\mu))+(\mu_1+\gamma)(\sigma+\mu)-\sigma\beta S_*,\\
c &= -(-\mu-\beta I_*)\ ((\mu_1+\gamma)(\sigma+\mu)-\sigma\beta S_*+\sigma I_*\beta^2 S_*.
\end{aligned}$$

Following this, by looking at the linearized system,

$$Z^{'}(t)=J(E_*)Z(t).$$

The stability of each equilibrium point, namely $E_*=E_0$ and $E_*=E^*$, can be evaluated. According to (3.2), the fundamental reproduction number, R_0, is the only value that determines this stability quality, as will be shown in the sections that follow. In the following two subsections, we will present two theorems that demonstrate the relationship between the local asymptotic stability of the equilibria and the value of R_0.

3.2.2. Stability of disease-free equilibrium E_0

This section will discuss the local stability of the disease-free equilibrium E_0. Initially, we select $E_*=E_0$. Consequently, the characteristic equation (3.4) becomes

$$(\lambda+\mu)^2\left[\lambda^2+\lambda[(\mu_1+\gamma)+(\sigma+\mu)]+(\mu_1+\gamma)(\sigma+\mu)-\sigma\beta\frac{A}{\mu}\right]=0. \tag{3.5}$$

Theorem 3.4. *(i) If $R_0<1$, then the disease-free equilibrium E_0 exhibits locally asymptotically stable.*
(ii) If $R_0>1$, then the equilibrium point E_0 becomes unstable [35].

3.2.3. Stability of endemic equilibrium E^*

This section will examine the local stability of the endemic equilibrium E^*. We suppose that $E_*=E^*=(S^*,E^*,I^*,R^*)$ at this position. Consequently, the characteristic equation (3.4) becomes

$$(\lambda+\mu)\ (\lambda^3+a\lambda^2+b\lambda+c)=0, \tag{3.6}$$

where

$$\begin{aligned}
a =&(\mu_1+\gamma)+\frac{\frac{A}{\mu}\beta\sigma}{R_0\ (\mu_1+\gamma)}+R_0\mu,\\
b =&\mu R_0\left((\mu+\gamma)+\frac{\sigma\beta A}{\mu(\mu_1+\gamma)R_0}\right),\\
c =&\sigma\beta A\left(\frac{R_0-1}{R_0}\right).
\end{aligned}$$

The following theorem follows as a result.

Table 1. The associated values and the parametric description [35].

Parameter	Description	Value
A	Population recruitment rate	Varied
β	Transmission rate	Varied
σ	Rate at which exposed individuals become infectious	0.25
μ	Natural mortality rate	0.07
α	Mortality rate due to the disease	0.07
γ	Natural recovery rate	0.07
S_0	Percentage of initial susceptible individuals	0.8
E_0	Percentage of initial exposed individuals	0.02
I_0	Percentage of initial infected individuals	0.07
R_0	Percentage of initial recovered individuals	0.01

Theorem 3.5. *If $R_0 > 1$, then the equilibrium point E^* is asymptotically stable* [35].

As a discretization approach for the SEIR model, we will employ Physics-Informed Neural Networks (PINNs). By leveraging PINNs, we can incorporate the underlying epidemiological dynamics directly into the learning process, ensuring that the model adheres to the governing differential equations. This method enables us to approximate the solution in a continuous manner while preserving the essential structural properties of the system, such as stability and conservation laws. Additionally, PINNs provide a flexible framework for handling complex boundary and initial conditions, making them well-suited for studying disease progression and control strategies in epidemiological models.

4. Physics-informed neural networks

In this section, we describe the structure of Physics-Informed Neural Networks (PINNs) for solving the SEIR epidemic model. The fundamental concept of PINNs is to incorporate prior knowledge in the form of physical laws or domain expertise typically expressed through ordinary or partial differential equations into a deep learning framework. This is achieved by computing derivatives of the neural network with respect to its input variables and model parameters; see [42] for further details. Consequently, the loss function not only minimizes data error but also reduces the residual of the differential equation using a least-squares approach.

4.1. The basics of neural networks for ODEs

We begin by analyzing the solution $u(t)$ of an ordinary differential equation (ODE), where the approximate solution for different values of t is expressed as $u_\theta \approx u$, with θ denoting a set of model parameters. For boundary value problems (BVPs), the variable t is typically reinterpreted from a time parameter, as used in initial value problems (IVPs), to a spatial coordinate parameter. A classical neural network that approximates the intended result allows us to write,

$$u_\theta(t) = (\mathcal{N}^L \circ \mathcal{N}^{L-1} .... \mathcal{N}^0)(t), \tag{4.1}$$

in this context, the operator $\circ$ denotes composition, and the trainable parameters of the network, including weight matrices and bias vectors are represented as $\theta = \{W^l, b^l\}_{l=1}^{L}$. Refer to [6] for additional details about the functions $\mathcal{N}^l$. The network architecture, illustrated in Figure 1, comprises $L+1$ layers, with neurons in each layer connected to those in the neighboring layers. The input layer is linked to $L-1$ hidden layers and contains the input variable t. In the schematic example shown in Figure 1, there are four hidden layers, each consisting of n neurons. This architecture culminates in an output layer that generates the solution u_θ. The objective is to modify the parameters θ so that u_θ closely matches the target solution $u(t)$. Furthermore, an activation function is essential for introducing non-linearity into the output of each neuron. In this research, the hyperbolic tangent function tanh, a commonly employed activation function, has been chosen for this role. The optimization problem involves minimizing a loss function,

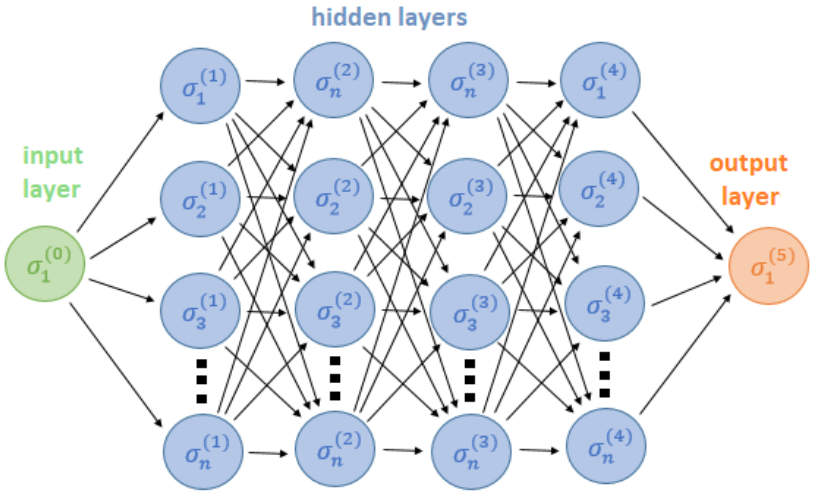

Figure 1. This schematic illustrates a typical neural network structure. The input layer consists of a single input variable, represented by one neuron as σ_1^0, which may, for instance, indicate a time coordinate. There are four hidden layers, each containing n neurons that connect to both the input layer and the output layer. The output layer features a single neuron, denoted as σ_1^5, which represents the desired solution u_θ.

which can be expressed as follows:

$$L_{\text{data}}(\theta) = \frac{1}{N_{\text{data}}} \sum_{i=1}^{N_{\text{data}}} \left| u_\theta(t_i) - u_{\text{data}}^i \right|^2, \tag{4.2}$$

where it is assumed that a set of N_{data} data points is available for the known solution at various time instances t_i (referred to as the training data, where $i = 1, \ldots, N_{\text{data}}$), including initial and/or boundary conditions.

4.2. The basics of PINNs for ODEs

An ordinary differential equation (ODE) with the residual form shown below will now be presented:

$$\mathcal{F}(t, u, \frac{du}{dt}, \frac{d^2u}{dt^2}, ...) = 0, \qquad t \in [t_0, T]. \tag{4.3}$$

The number of initial and/or boundary conditions necessary to solve the equation is contingent

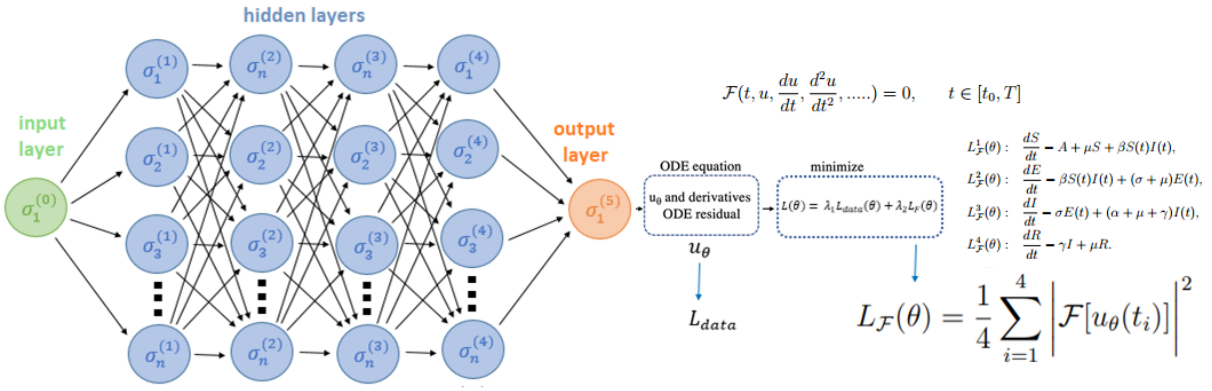

Figure 2. A Physics-Informed Neural Network (PINN) that is intended to estimate the solution of an ordinary differential equation (ODE) is shown in this picture. The neural network architecture shown in the previous figure is employed to assess the residual of the ordinary differential equation (ODE) by utilizing u_θ and its associated derivatives. After integrating two partial loss functions, L_{data} and $L_{\mathcal{F}}$, a comprehensive loss function is produced. It is then minimized and weighted as needed (as described in the text).

upon the specific problem being considered and the order of the equation itself. It is noteworthy that for an ordinary differential equation (ODE) of order n equal to or greater than two, one can also employ an equivalent system of n equations (as detailed [6]). The fundamental principles of Physics-Informed Neural Networks (PINNs) in their original formulation rely on incorporating a secondary loss function defined as follows:

$$L_{\mathcal{F}}(\theta)=\frac{1}{N_c}\sum_{i=1}^{N_c}\left|\mathcal{F}[u_\theta(t_i)]\right|^2, \tag{4.4}$$

which needs to be assessed at a collection of N_c points, also referred to as collocation points, which don't have to line up with the training data points. In our work we define

$$\begin{aligned}
L^1_{\mathcal{F}}(\theta) &: \frac{dS}{dt}-A+\mu S+\beta S(t)I(t),\\
L^2_{\mathcal{F}}(\theta) &: \frac{dE}{dt}-\beta S(t)I(t)+(\sigma+\mu)E(t),\\
L^3_{\mathcal{F}}(\theta) &: \frac{dI}{dt}-\sigma E(t)+(\alpha+\mu+\gamma)I(t),\\
L^4_{\mathcal{F}}(\theta) &: \frac{dR}{dt}-\gamma I+\mu R,
\end{aligned}$$

so the here

$$L_{\mathcal{F}}(\theta)=\frac{1}{4}\sum_{i=1}^{4}\left|\mathcal{F}[u_\theta(t_i)]\right|^2, \tag{4.5}$$

where $\theta=(S,E,I,R)$. Interestingly, automatic differentiation allows for precise computation of the differential operators in $L_{\mathcal{F}}$ and $\mathcal{F}$ at the collocation points. In order to calculate derivatives with regard to the network weights (i.e., θ), which are essential for completing the optimization process (as explained below), this automatic differentiation technique is used. This approach

enables the creation of derivatives with machine precision, in contrast to conventional numerical approaches. To make these processes easier, utilizing a fully connected neural network (FCN) built with PyTorch open-source software in our work. In this study, mostly the architecture of the neural network comprises four hidden layers, with each layer featuring 64 neurons, allowing the model to adeptly capture and represent the intricate dynamics of the SEIR system.

The expression for a composite total loss function is so

$$L(\theta) = \lambda_1 L_{\text{data}}(\theta) + \lambda_2 L_{\mathcal{F}}(\theta), \tag{4.6}$$

in which the potential discrepancies between the partial losses during the training process are minimized by selecting the hyperparameters λ_1 and λ_2 with the best possible values. These weights can be adjusted automatically or manually. To keep things simple, the weight parameters, such as λ_1 and λ_2, are decided by the particular situation. To reach convergence, a gradient descent method is used, aiming for either a predetermined accuracy or a maximum number of iterations, as explained below:

$$\theta^{k+1} = \theta^k - \eta \nabla_\theta L(\theta^k). \tag{4.7}$$

The goal of the k-th iteration, which is sometimes referred to as an epoch in the literature, is to minimize the loss function so that

$$\theta^* = \arg\min_\theta L(\theta), \tag{4.8}$$

with (η) serving as the learning rate parameter. In this work, we apply the well-known Adam optimizer. The derivatives (i.e., ∇_θ) pertaining to the neural network parameters, such as weights and biases, are calculated using a common automatic differentiation approach [42]. A schematic representation of the Physics-Informed Neural Networks (PINNs) is presented in Figure 2. It is crucial to emphasize in this image that for partial differential equations (PDEs) that exhibit spatiotemporal relationships, two neurons should be used in place of the single input neuron, which represents a time or spatial coordinate for ODEs (x, t). Furthermore, the output neuron needs to be swapped out with n neurons, each of which represents one of the n solution variables that need to be learned, when working with a set of n differential equations.

5. The experiments

In this section, we present some results derived using Physics-Informed Neural Networks (PINNs) to illustrate the theoretical findings we have listed above. The graphical results for the SEIR model have been generated using PINNs to highlight the dynamics of the system (2.1).

5.1. Parameters of the PINNs

Here is a detailed description of the parameters involved in the PINNs implementation for simulating the SEIR model:

- The framework used is PyTorch, with the model type being a Fully Connected Network (FCN).
- CPU Utilization: AMD A12-9720P RADEON R7, 12 COMPUTE CORES 4C+8G 2.70 GHz.

Table 2. The associated values and the parametric description.

Parameter description	Grid parameter	Finest parameter
Input units	1	1
Hiden layers	4, 19, 33	4
Neuron units per hidden layers	64, 100, 150	64
Output units	4	4
Learning rate	0.01, 0.0001, 0.00001	0.01
Batch Size	200	200
Number of Epochs	5000, 10000, 14000, 15000, 40000, 50000	5000
Optimizer	Adam	Adam
Lambda Values	$\lambda_1 = 0.0001, 0.001, 0.01, 0.1, 0.5, 1.0, 5,$ $\lambda_2 = 0.8, 1.0, 1.996, 2.8958.999, 9.9$	$\lambda_1 = 0.01, \lambda_2 = 1.0$
Weight Dacay	0.001	0.001

These parameters collectively contribute to the performance and effectiveness of the PINNs in simulating the SEIR epidemic model. Adjusting these parameters based on the specific dataset and problem context can enhance the model's predictive capabilities and stability.

We also compared the results of our PINNs with the results of the Runge-Kutta fourth-order (RK4). In the PINNs and RK4 simulations, the SEIR parameters used are described in Table 1.

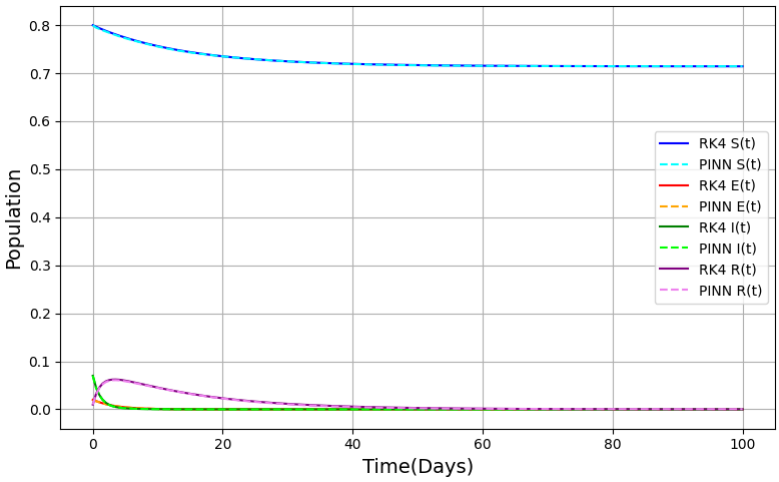

Figure 3. Results by using RK4 and PINNs.

Remark 5.1. If we set $A = 0.05$ and $\beta = 0.01$, this results in $R_0 = 0.0266$. According to

Theorem 3.4, the disease-free equilibrium $E_0^{RK4} = (0.7144, 0, 0, 0.0001)$ is locally asymptotically stable. Utilizing the PINNs, we compute $E_0^{PINN} = (0.7145,\ 0,\ 0,\ 0.0004)$. This implies that the disease dies out (see Figure 3). In Figure 3, it is noted that the number of susceptible individuals declines over the initial 10 days and subsequently stabilizes at a constant value. The number of people who are infected, exposed, and eliminated decreases to zero, as this graph also demonstrates. After 10 days, the disease appears to be eradicated from the host population.

Next, if we choose $A = 0.09$ and $\beta = 0.9$, then we have $R_0 = 4.3048$. According to Theorem 3.5, the endemic equilibrium $E^{*RK4} = (0.2987, 0.2159, 0.2570, 0.2569)$ is locally asymptotically stable, and using PINNs, we find $E^{*PINN} = 0.2997, 0.2153, 0.2559, 0.2559)$. So the PINNs offers a significantly clearer and more detailed solution than RK4.

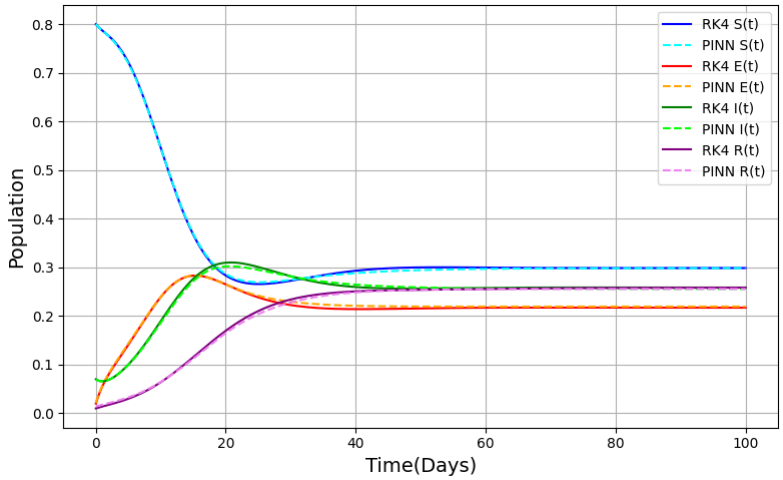

Figure 4. Results by using RK4 and PINNs.

Remark 5.2. Figure 4 demonstrates the local stability of the endemic equilibrium points E^*_{RK4} and E^*_{PINN} when the basic reproduction number is $R_0 = 4.3048$. Biologically, this high value of R_0 indicates that each infected individual, on average, transmits the disease to more than four others, leading to sustained transmission. The figure shows that after approximately 20 days, the number of infected individuals stabilizes, suggesting that the disease becomes endemic within the population rather than dying out. This reflects a persistent burden of infection, which could imply ongoing public health challenges. While both RK4 and PINNs capture this behavior, the PINNs approach provides a smoother and more accurate representation of the epidemic dynamics, which can be particularly useful for biological interpretation and prediction.

5.2. Global stability of two equilibrium points

In this section, we broaden the scope of the research presented in [24–26] by eliminating any limitations regarding the population size. We will now investigate the global stability of the two equilibrium points of the system described by (2.1) using the generalized Lyapunov's theorem introduced by [7], without imposing any restrictions on population size. We will show that if $R_0 \leq 1$, then the equilibrium point E_0 is globally asymptotically stable; and if $R_0 > 1$, the equilibrium point E^* is globally asymptotically stable.

5.2.1. Global stability of disease-free equilibrium E_0

Theorem 5.1. *The disease-free equilibrium point E_0 is globally asymptotically stable if $R_0 \leq 1$* [35].

5.2.2. Global stability of the endemic equilibrium

The endemic equilibrium E^* is shown to be globally asymptotically stable in this paragraph by building a suitable Lyapunov function, provided that $R_0 > 1$.

Theorem 5.2. *According to* [35]*, the equilibrium point E^* is globally asymptotically stable if $R_0 > 1$.*

5.2.3. Experimental results for global stability

To show that the equilibrium points are globally stable, we will modify the initial conditions of the system defined by (2.1). This section will demonstrate the evolution of the system's solutions across four distinct initial conditions, beginning with the disease-free equilibrium. In this case, by selecting $A = 0.05$ and $\beta = 0.09$, we find that $R_0 = 0.2392$. According to Theorem 5.1, the disease-free equilibrium $E_0^{RK4} = (0.7142, 0, 0, 0.0001)$ is globally asymptotically stable. In Figure 5, using the Physics-Informed Neural Networks (PINNs), we find $E_0^{PINN} = (0.7143, 0, 0, 0)$. After 60 days, it is shown that the system stabilizes and moves closer to the disease-free equilibrium, suggesting that this equilibrium is asymptotically stable globally. In this scenario, the disease has effectively disappeared from the host population.

Next, if we choose $A = 0.05$ and $\beta = 0.9$, we have $R_0 = 2.3916$. Therefore, according to Theorem 5.2, the endemic equilibrium points E^{*RK4} and E^{*PINN} are globally asymptotically stable, as evidenced by the results derived from the RK4 and PINNs (refer to Figure 6). In scenarios where the disease remains prevalent in the population, it is essential to develop a control law tailored for high-risk areas with a greater density of exposed individuals. The main objective of this tailored strategy is to efficiently mitigate the spread of the disease in areas where the risk is highest. This could involve the implementation of measures such as targeted testing, isolation, quarantine, and potentially an augmentation of health care resources. It is essential to underscore that the development of this control law must be carried out thoughtfully, with the option of incorporating backstepping methods, while maintaining a particular focus on the compartment associated with exposed individuals.

Remark 5.3. Figure 5 illustrates the global asymptotic stability of the disease-free equilibrium points E_0^{RK4} and E_0^{PINN} obtained via the RK4 method and PINNs, respectively, for a basic reproduction number $R_0 = 0.2392$. Biologically, since $R_0 < 1$, the disease cannot sustain itself within the population and eventually dies out. This is reflected in the trajectories converging to the disease-free equilibrium, indicating successful eradication of the infection over time.

In contrast, Figure 6 examines the global asymptotic stability of the endemic equilibrium for $R_0 = 2.3916$, where both methods predict disease persistence. The RK4 method yields the equilibrium state $E^*_{\mathrm{RK4}} = (0.2988, 0.0909, 0.1082, 0.1082)$, while the PINNs approach estimates $E^*_{\mathrm{PINN}} = (0.3018, 0.0895, 0.1066, 0.1071$. These results indicate that a significant portion of the population remains infected or exposed in the long term, consistent with the behavior of an endemic disease when $R_0 > 1$. Notably, the PINNs solution is smoother and more detailed, highlighting its advantage in capturing subtle dynamics that traditional numerical solvers like

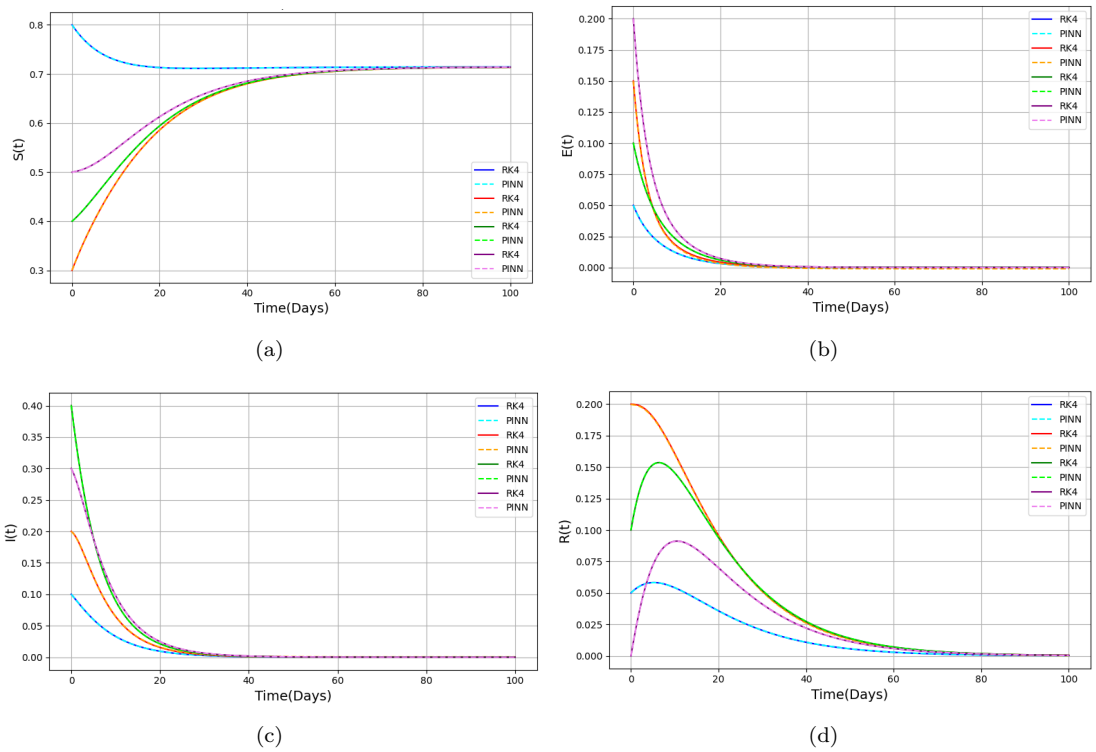

Figure 5. Comparison of results obtained using RK4 and PINNs.

RK4 might overlook. This underscores the effectiveness of our PINNs-based method in providing biologically meaningful and computationally accurate insights into epidemic behavior.

5.3. Control of the SEIR model

The backstepping control method, introduced in the 1990s by Petar Kokotovic, is a nonlinear control technique designed to solve the control problem in dynamic systems [22, 27]. This approach offers an alternative to linearisation, which is commonly used in nonlinear control. Backstepping's core concept involves a recursive synthesis of the control law, breaking the system down into components, with some treated as 'virtual controls'. Intermediate control laws are then developed for these virtual controls, making the system more manageable. Unlike input-output or state-space linearisation, which can lead to the loss of vital information about system nonlinearities, backstepping preserves these nonlinear characteristics. It's particularly well-suited for triangular nonlinear systems, often referred to as 'strict feedback systems [47, 48]. This method is less restrictive and doesn't impose linearity on the system, making it a valuable tool in the field of nonlinear control [23]. Furthermore, the backstepping control method is known for its robustness in handling systems with unknown or uncertain parameters. It demonstrates the ability to adapt to parameter variations, ensure system stability, reject disturbances, and withstand robust stability analysis. These attributes make it a valuable approach for effectively controlling complex systems in real-world applications.

In the SEIR model, the measurability of each compartment's state varies based on data availability and the specific characteristics of the disease being studied. While 'Infectious' individuals are often measurable through confirmed cases and related data, 'Susceptible' individuals

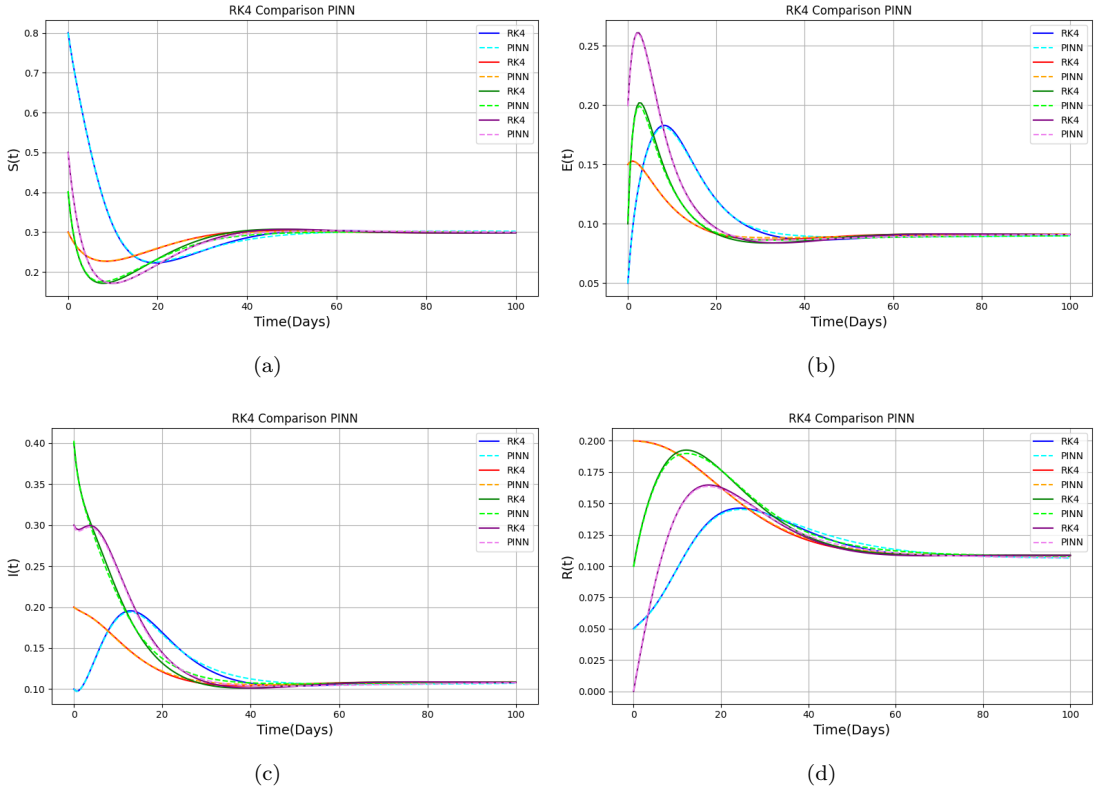

Figure 6. Comparison of results obtained using RK4 and PINNs.

are generally not directly measurable but can be estimated using population data and reported cases. Measuring 'Exposed' individuals is challenging due to their lack of symptoms and the need for robust contact tracing. 'Removed' individuals, including those who have recovered or died, are generally measurable. Data quality, such as underreporting and testing variations, poses a significant challenge. Consequently, we can use statistical estimation techniques to derive estimates for each compartment, ensuring a better understanding of disease transmission and aiding public health decisions. Furthermore, when dealing with partially unknown states in the SEIR model or any similar epidemiological modelling, the use of observers or state estimators becomes crucial. These techniques play a vital role in estimating unobservable states, such as the number of exposed individuals, given the inherent challenges in direct measurement. Observers leverage available data and model dynamics to provide informed estimates, which are invaluable for monitoring disease spread, guiding control measures, and informing public health strategies. In scenarios where precise data are lacking, these tools bridge the gap, enabling more accurate modelling and decision-making. Additionally, determining exposed individuals in reality involves the use of various methods and data sources tailored to the specific disease. Common approaches include contact tracing to identify exposed individuals, analysing epidemiological data to estimate exposed cases, using mathematical models to refine these estimates, employing laboratory tests to detect past exposures, conducting cohort studies to assess the risk of infection, collecting information on recent travel and exposures, and conducting field epidemiological investigations to trace the sources of infection. The accuracy of determining exposed individuals depends on data availability and the nature of the disease, and a combination of these methods is often

required for more precise estimations. Swift identification of exposed individuals is crucial for effective epidemic control and controlling high-risk areas, where potentially exposed individuals are concentrated, is indeed crucial in epidemic management. These areas can serve as hotspots for infection, and swift monitoring, identification, and isolation of exposed individuals are vital to prevent further disease transmission. By directing resources toward high-risk areas using control measures such as testing, quarantine, and targeted treatment campaigns, we can more effectively mitigate the spread of the disease and enhance public health protection.

In this section, we develop a controller that uses the backstepping technique to track and stabilize the SEIR model. The backstepping method is introduced as a technique for controlling the SEIR model where $R_0 > 1$, the fundamental reproduction number. In this regard, the method is a helpful tool for creating a control law that maintains the system at the point of disease-free equilibrium, facilitating the removal of the disease from the population. The backstepping technique permits the control of the chaotic dynamics of the SEIR model, guiding it towards any predetermined trajectory. A notable benefit of this approach is its flexibility, which allows for the design of a control law that fulfills both stabilization and tracking objectives while reducing the amount of control effort required. This section's first half is devoted to stabilization, while the second part employs the backstepping method to identify the control rule that allows our SEIR model to follow any given trajectory.

5.3.1. Backstepping control

By introducing a control input μ_2 to the second equation of the system specified by (2.1), we stabilize the SEIR model at the disease-free equilibrium $E_0 = \left(\frac{A}{\mu}, 0, 0, 0\right)$ in order to successfully eliminate the disease from the population. Then the controlled SEIR model becomes as follows:

$$\begin{aligned}
\frac{dS}{dt} &= A - \mu S(t) - \beta S(t)I(t),\\
\frac{dE}{dt} &= \beta S(t)I(t) - (\sigma + \mu)E(t) + \mu_2,\\
\frac{dI}{dt} &= \sigma E(t) - (\mu_1 + \gamma)I(t),\\
\frac{dR}{dt} &= \gamma I(t) - \mu R(t).
\end{aligned} \tag{5.1}$$

The stability of the disease-free equilibrium point indicates that the disease has been totally eliminated from the population, whereas the stability of the endemic equilibrium point indicates that the disease is still present and persistent in the population. Finding a control law that guides the system toward stability at the point of disease-free equilibrium makes sense as a result. Our goal is to find a control law μ_2 that provides asymptotic stability to the system represented by (5.1) at the disease-free equilibrium point E_0. To do this, we will start by using the backstepping method to create the control input μ_2.

Step 1. Let $S = Z_1$ and I be the virtual control of Z_1-subsystem and $I = \alpha_1(Z_1)$. So, we have

$$\dot{S} = \dot{Z}_1 = A - \mu Z_1 - \beta Z_1 \alpha_1.$$

To achieve asymptotic stabilization of the $Z_1 -$ subsystem, we need to determine α_1 by considering the following Lyapunov function

$$V_1 = Z_1 - \frac{A}{\mu} - \frac{A}{\mu} \ln\left(\frac{\mu Z_1}{A}\right).$$

On the trajectory, the derivative of V_1 is then provided by

$$\begin{aligned}\dot{V}_1 &= \dot{Z}_1 - \frac{A}{\mu}\left(\frac{\dot{Z}_1}{Z_1}\right)\\ &= \dot{Z}_1 - \frac{A}{\mu Z_1}(\dot{Z}_1)\\ &= (A - \mu Z_1 - \beta Z_1\alpha_1)\left(1 - \frac{A}{\mu Z_1}\right),\end{aligned}$$

where α_1 is the input control

$$\begin{aligned}&= -(A - \mu Z_1 - \beta Z_1\alpha_1)\left(\frac{A - \mu Z_1}{\mu Z_1}\right)\\ &= -\frac{(A - \mu Z_1)^2}{\mu Z_1} + \frac{\beta\alpha_1 Z_1}{\mu Z_1}(A - \mu Z_1)\\ &= -\frac{1}{\mu Z_1}(A - \mu Z_1)^2 + \frac{\beta}{\mu}(A - \mu Z_1)\alpha_1.\end{aligned}$$

By selecting $\alpha_1 = 0$, we observe that $\dot{V} < 0$. By demonstrating that the state Z_1 approaches the equilibrium point $\frac{A}{\mu}$ as $t \to \infty$ tends to infinity, this validates the asymptotic stability of the $Z_1 -$ subsystem.

Next, let Z_2 be the error between I and α_1. Then $Z_2 = I - \alpha_1 = I$ and we have the following $(Z_1, Z_2) -$ subsystem

$$\begin{aligned}\dot{Z}_1 &= A - \mu Z_1 - \beta Z_1 Z_2,\\ \dot{Z}_2 &= \sigma E - (\mu_1 + \gamma)Z_2.\end{aligned} \tag{5.2}$$

Step 2. Let $E = \alpha_2(Z_1, Z_2)$ be the virtual control of the $(Z_1, Z_2) -$ subsystem. In this step, we seek to find a virtual control law α_2, which stabilises the $(Z_1, Z_2) -$ subsystem towards the equilibrium point $(\frac{A}{\mu}, 0)$. In order to accomplish this, The Lyapunov function V_2 can be chosen in the manner described below:

$$V_2 = V_1 + \frac{1}{2}Z_2^2.$$

Accordingly, the time derivative of V_2 along the $(Z_1, Z_2) -$subsystem's trajectory is derived from

$$\begin{aligned}\dot{V}_2 &= \dot{V}_1 + Z_2\dot{Z}_2\\ &= -\frac{1}{\mu Z_1}(A - \mu Z_1)^2 - (\mu_1 + \gamma)Z_2^2 + Z_2\left(\sigma\alpha_2 + \frac{\beta}{\mu}(A - \mu Z_1)\right).\end{aligned}$$

If we choose $\alpha_2 = \frac{\beta}{\sigma\mu}(\mu Z_1 - A)$, then we have $\dot{V}_2 < 0$. This suggests that the $(Z_1, Z_2) -$ subsystem's equilibrium point $(\frac{A}{\mu}, 0)$ is asymptotically stable.

Next, let Z_3 be the error between E and α_2. Then, $Z_3 = E - \alpha_2$, and we have the following: $(Z_1, Z_2, Z_3) -$ subsystem.

$$\begin{aligned}\dot{Z}_1 &= A - \mu Z_1 - \beta Z_1 Z_2,\\ \dot{Z}_2 &= \sigma Z_3 + \beta Z_1 - \frac{\beta}{\mu}A - (\mu_1 + \gamma)Z_2,\end{aligned} \tag{5.3}$$

$$\dot{Z}_3 = -\beta Z_1 - (\sigma+\mu)Z_3 + \beta Z_1 Z_2\left(1+\frac{\beta}{\sigma}\right) + \frac{\beta}{\mu}A + \mu_2.$$

Step 3. In this step, we must seek a control law μ_2 which stabilies the $(Z_1, Z_2, Z_3)-$subsystem to the equilibrium point $(\frac{A}{\mu}, 0, 0)$. First of all, we consider the following Lyapunov function

$$V_3 = V_2 + \frac{1}{2}Z_3^2.$$

Next, the time derivative of V_3 along the $(Z_1, Z_2, Z_3)-$subsystem's trajectory is provided by

$$\begin{aligned}
\dot{V}_3 &= \dot{V}_2 + Z_3\dot{Z}_3 \\
&= \dot{V}_1 + Z_2\dot{Z}_2 + Z_3\dot{Z}_3 \\
&= -\frac{1}{\mu Z_1}(A-\mu Z_1)^2 + \frac{\beta Z_1 Z_2}{\mu Z_1}(A-\mu Z_1) + \sigma Z_2 Z_3 + \beta Z_1 Z_2 - \frac{A\beta}{\mu}Z_2 \\
&\quad - (\mu_1+\gamma)Z_2^2 + Z_3\bigg[-\beta Z_1 - (\gamma+\mu)Z_3 + \beta Z_1 Z_2\left(1+\frac{\beta}{\sigma}\right) + \frac{\beta}{\mu}A + \mu_2\bigg] \\
&= -\frac{1}{\mu Z_1}(A-\mu Z_1)^2 - (\mu_1+\gamma)Z_2^2 - (\sigma+\mu)Z_3^2 \\
&\quad + Z_3\bigg[-\beta Z_1 + \sigma Z_2 + \beta Z_1 Z_2\left(1+\frac{\beta}{\sigma}\right) + \frac{\beta}{\mu}A + \mu_2\bigg].
\end{aligned} \tag{5.4}$$

If we choose $\mu_2 = \beta Z_1 - \sigma Z_2 - \frac{\beta}{\mu}A - \beta Z_1 Z_2(1+\frac{\beta}{\sigma})$, then we get $\dot{V}_3 < 0$. For the $(Z_1, Z_2, Z_3)-$subsystem, consequently, the equilibrium point $(\frac{A}{\mu}, 0, 0)$ is globally asymptotically stable. Since $Z_1 = S$, $Z_2 = I$ and $Z_3 = E - \frac{\beta}{\sigma\mu}(\mu Z_1 - A)$, then this implies that S, I and E converge asymptotically to $\frac{A}{\mu}$, 0 and 0, respectively. Moreover, from the last equation of system (5.1) and since I converges to zero, then we can deduce that the state R converges asymptotically to zero.

Consequently, we have developed a control mechanism μ_2, that eliminates sickness by successfully stabilizing the system toward the disease-free equilibrium point. This protocol is designed based on the proportions of susceptible, exposed, and infectious individuals within the population. It precisely dictates the required percentage of individuals to be removed from the group of exposed individuals, through quarantine, isolation, treatment or other medical intervention. In addition, the adaptability of this protocol to high-risk areas, where a significant proportion of exposed people often reside, improves its effectiveness and makes it able to completely eradicate the illness from the populace by targeting high-risk areas and vulnerable regions.

5.3.2. Experimental results for backstepping

Here, we demonstrate the effectiveness of the backstepping technique in stabilizing our SEIR model in scenarios. If there is instability in the disease-free equilibrium, or when $R_0 > 1$. The system is stabilized and brought closer to the disease-free equilibrium by using the previously mentioned control law μ_2. In actuality, though, this is crucial because we have discovered a control law that enables us to completely wipe the illness from the host population.

For experiments, we will employ the identical parameter settings as those presented in Table 1. Additionally, to ensure the positivity of our system, we impose a constraint on the number of exposed individuals E, requiring it to remain positive and greater than a minimum value $E_{min} = 0$. Our control law is applied only under these conditions. If its implementation leads

to a negative count of exposed individuals, we reset E to zero. This approach mirrors real-world scenarios where control measures are implemented based on the presence of exposed individuals, ensuring both practicality and realism. Subsequently, if we choose $A = 0.09$, $\beta = 0.9$ and $\mu = 0.1$, then we get $R_0 = 2.4107$. Consequently, according to Theorem 5.2, the disease is expected to establish itself in the population. Consequently, after 30 days, if we apply our previously determined control law μ_2, we observe that the system tends to converge toward the disease-free equilibrium. Consequently, our community will be free of the sickness (see Figure 7).

Furthermore, to evaluate the effectiveness of our control law, we implement it between day 30 and day 60, and then discontinue its application after 60 days. We observe that without this intervention, the disease undergoes a resurgence and becomes established in the population, as illustrated in Figure 8.

Moreover, to evaluate the robustness of our control law μ_1, we introduced a disturbance with a value of $\delta = 0.2$ in system (5.1). In this scenario, we applied a modified law $\mu_1' = \mu_1 + \delta$, then compared the results obtained with the solutions of the system (5.1), with and without control. This approach allows us to test the control law's effectiveness in maintaining satisfactory performance even when faced with disturbances. Figure 9 demonstrates that the results obtained with a control law disturbance of value $\delta = 0.2$ remain sufficiently close to the solutions with exact control and significantly out perform solutions without control.

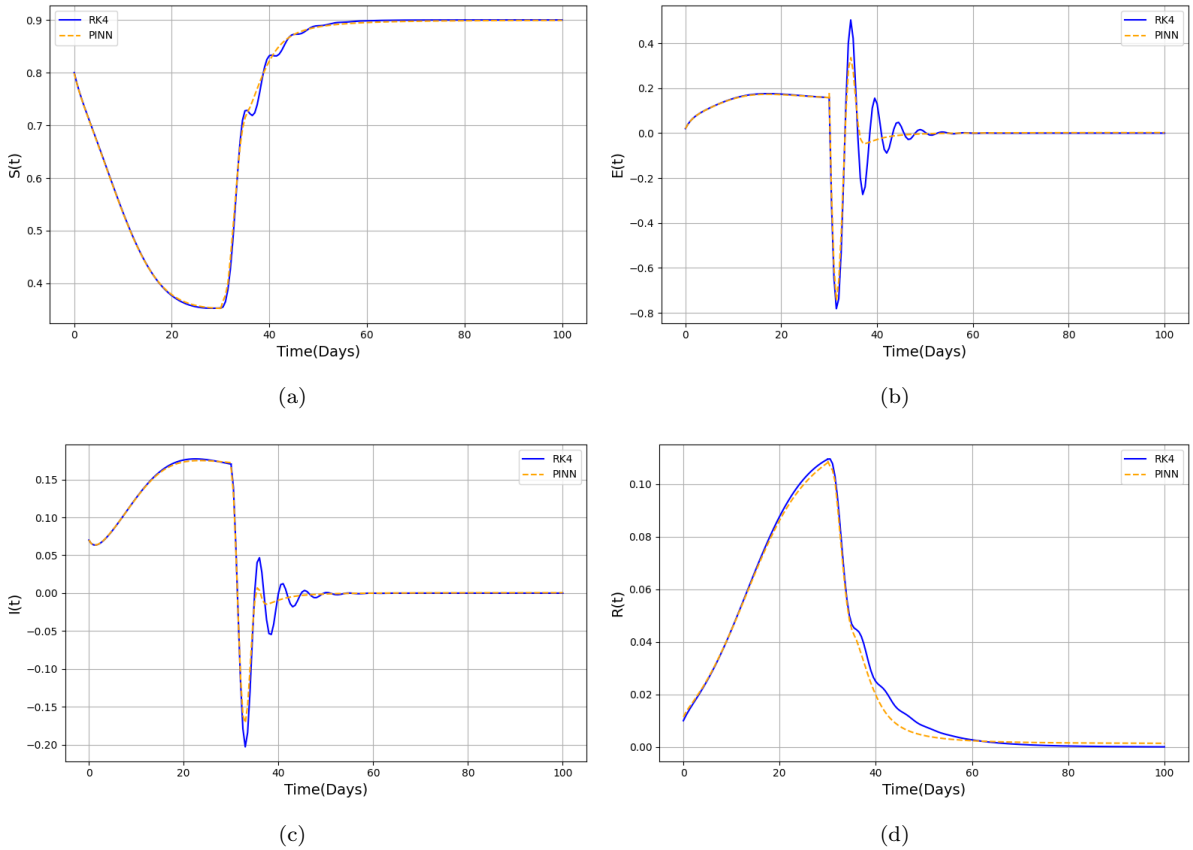

Figure 7. Comparison of results obtained using RK4 and PINNs.

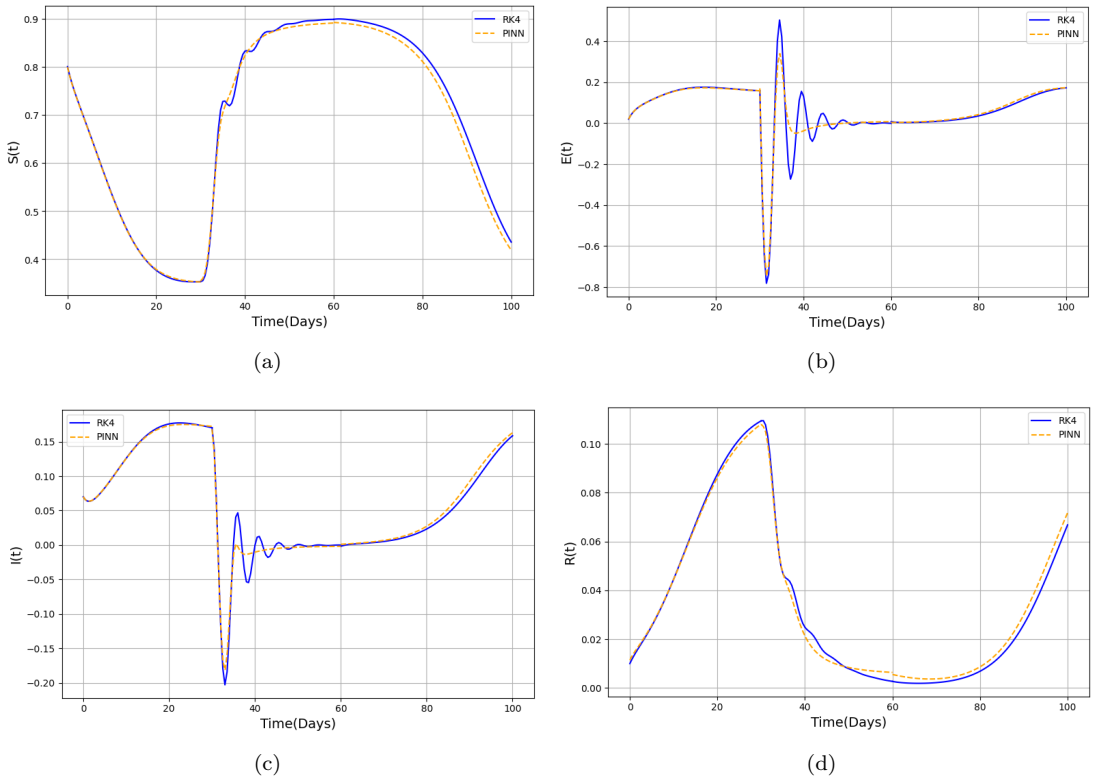

Figure 8. Comparison of results obtained using RK4 and PINNs.

Remark 5.4. Figure 7 illustrates how the SEIR model dynamics stabilize around the 30-day mark when the control law μ_2 is applied. Under the RK4 method, the solution converges to the disease-free equilibrium point $E_0^{\text{RK4}} = (0.9, 0, 0, 0)$, while the PINNs approach estimates a slightly perturbed but biologically similar equilibrium $E_0^{\text{PINN}} = (0.9009, 0.0008, 0.0009, 0.0001)$. Despite the basic reproduction number being $R_0 = 2.4107 > 1$, which would typically indicate disease persistence, the application of the control law μ_2 is evidently effective in driving the infection toward eradication. Biologically, this suggests that strong or timely interventions can overcome high transmission potential and steer the population toward a disease-free state.

Examining Figure 8, we observe the effect of continuing the control law μ_2 from day 30 to day 60. The system stabilizes toward an endemic equilibrium, denoted by E^*_{RK4} and E^*_{PINN} for the RK4 and PINNs methods, respectively. This indicates that while the control reduces the infection burden, it may not be sufficient to completely eliminate the disease under these conditions. Notably, the PINNs solution provides a more refined and detailed representation of the epidemic trajectory compared to RK4, capturing subtle transitions in the model dynamics. These results demonstrate the enhanced capability of PINNs in offering biologically meaningful and computationally accurate solutions, reinforcing their effectiveness over traditional numerical methods.

Remark 5.5. Examining Figure 9, it becomes evident that when a disturbance level of $\delta = 0.2$ is introduced, the solutions of system (5.1) exhibit a more favorable disease progression compared

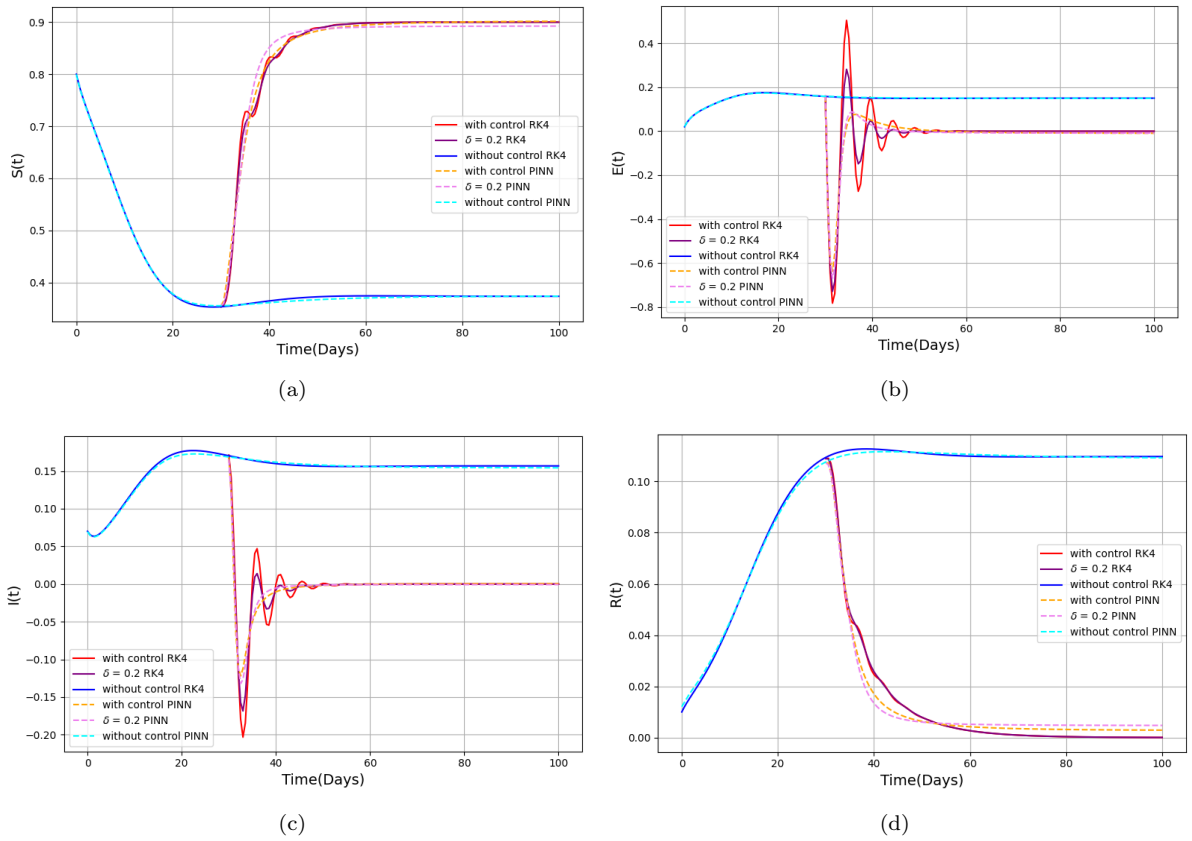

Figure 9. Comparison of results obtained using RK4 and PINNs.

to the scenario without any control. Biologically, this suggests that even in the presence of disturbances such as variability in population behavior or external factors. The applied control mechanisms can still effectively mitigate the spread of the disease. The infection levels remain lower and converge more rapidly under control, indicating improved disease management.

Moreover, the PINNs approach yields a significantly clearer and more detailed solution compared to the RK4 method, capturing fine-grained variations in the dynamics that may be critical for understanding transmission trends. This highlights the robustness and accuracy of the PINNs framework in modeling real-world epidemic behavior, especially under non-ideal conditions. The results support the use of PINNs as a powerful tool for simulating disease control strategies in the presence of uncertainty.

5.4. Tracking of SEIR model

The backstepping technique is used in this section to generate a control rule to synchronize two identical SEIR models. First, we rewrite the SIR model (2.1) in the appropriate form to apply the backstepping method. Thus, we put $x_1 = R$, $x_2 = I$, $x_3 = E$, and $x_4 = S$, then we obtain the following system

$$\begin{aligned}\dot{x}_1 &= \gamma x_2 - \mu x_1,\\ \dot{x}_2 &= \sigma x_3 - (\mu_1 + \gamma)x_2,\end{aligned}$$

$$\begin{aligned}\dot{x}_3 &= \beta x_4 x_2 - (\sigma + \mu)x_3,\\ \dot{x}_4 &= A - \mu x_4 - \beta x_4 x_2.\end{aligned} \tag{5.5}$$

Next, we consider system (5.5) as the drive system, which serves as the reference trajectory to investigate the synchronization behavior within the SEIR model. Then, the response system is

$$\begin{aligned}\dot{y}_1 &= \gamma y_2 - \mu y_1,\\ \dot{y}_2 &= \sigma y_3 - (\mu_1 + \gamma)y_2,\\ \dot{y}_3 &= \beta y_4 y_2 - (\sigma + \mu)y_3 + \mu_2,\\ \dot{y}_4 &= A - \mu y_4 - \beta y_4 y_2,\end{aligned} \tag{5.6}$$

where the input for control is μ_2.

Our next objective is to determine the control input μ_2 that enables synchronization of the response system (5.6) with the drive system (5.5). For the states that exist between the variables of the driving and response systems, we make the following assumptions:

$$\begin{aligned}e_1 &= y_1 - x_1,\\ e_2 &= y_2 - x_2,\\ e_3 &= y_3 - x_3,\\ e_4 &= y_4 - x_4.\end{aligned} \tag{5.7}$$

After all calculation done we will end up with the following system:

$$\begin{aligned}\dot{e}_1 &= \gamma e_2 - \mu e_1,\\ \dot{e}_2 &= \sigma e_3 - (\mu_1 + \gamma)e_2,\\ \dot{e}_3 &= -(\sigma + \mu)e_3 + \beta x_4 e_2 + \beta y_2 e_4 + \mu_2,\\ \dot{e}_4 &= \mu e_4 - \beta y_4 e_2 - \beta x_2 e_4.\end{aligned} \tag{5.8}$$

Our goal is to develop a control law μ_2 that ensures the convergence of the vector $e = [e_1, e_2, e_3, e_4]^T$ to zero as $t \to \infty$. This convergence indicates that the trajectories of the response system (5.6) asymptotically align with those of the drive system (5.5). We will now proceed to design the control input μ_2 using the backstepping method.

Step 1. Assume $z_1 = e_1$. Its derivative is then provided by:

$$\dot{z}_1 = \dot{e}_1 = \gamma e_2 - \mu z_1,$$

where the virtual control input is $e_2 = \alpha_1(z_1)$.

To construct α_1 that guarantees the $z_1 -$ subsystem's asymptotic stability, we take into account the Lyapunov function, which is provided by:

$$V_1 = \frac{1}{2} z_1^2.$$

As a result, the V_1 time derivative along the $z_1 -$ subsystem trajectory is

$$\begin{aligned}\dot{V}_1 &= z_1 \dot{z}_1,\\ &= -\mu z_1^2 + \gamma \alpha_1 z_1.\end{aligned}$$

If we choose $\alpha_1 = 0$, then $\dot{V}_1 = -\mu z_1^2$. This leads to the asymptotic stability of the z_1-subsystem.

The error between e_2 and α_1 is thus denoted by z_2. Consequently, we may derive the subsequent $(z_1, z_2) -$ subsystem

$$\begin{aligned} \dot{z}_1 &= -\mu z_1 + \gamma z_2, \\ \dot{z}_2 &= \sigma e_3 - (\mu_1 + \gamma) z_2. \end{aligned} \tag{5.9}$$

Step 2. Here we take $e_3 = \alpha_2(z_1, z_2)$ as virtual control of $(z_1, z_2) -$ subsystem. We then take into account the following Lyapunov function

$$V_2 = V_1 + \frac{1}{2} z_2^2.$$

The outcome of computing the time derivative of V_2 along the trajectory of the $(z_1, z_2) -$ subsystem is

$$\begin{aligned} \dot{V}_2 &= \dot{V}_1 + z_2 \dot{z}_2 \\ &= -\mu z_1^2 + z_2(\sigma \alpha_2 - (\mu_1 + \gamma) z_2) + \gamma z_1 z_2 \\ &= -\mu z_1^2 - (\mu_1 + \gamma) z_2^2 + \sigma \alpha_2 z_2 + \gamma z_1 z_2. \end{aligned} \tag{5.10}$$

If we choose $\alpha_2 = \frac{-\gamma}{\sigma} z_1$, then this ensures the asymptotic stability of the (z_1, z_2)-subsystem.

Afterwards, let z_3 be the error dynamic between e_3 and α_2. So, we have $z_3 = e_3 - \alpha_2$. Thus, we get the following $(z_1, z_2, z_3) -$ susbsystem

$$\begin{aligned} \dot{z}_1 &= -\mu z_1 + \gamma z_2, \\ \dot{z}_2 &= -(\mu_1 + \gamma) z_2 + \gamma z_1, \\ \dot{z}_3 &= -(\sigma + \mu) z_3 + \left(\beta x_4 + \frac{\gamma^2}{\sigma} \right) z_2 + \gamma z_1 + \beta y_2 e_4 + \mu_2. \end{aligned} \tag{5.11}$$

Step 3. At this point, we are looking for a control law μ_2 that guarantees the asymptotic stability of the $(z_1, z_2, z_3) -$ susbsystem. The following Lyapunov function can be taken into consideration first in order to achieve this.

$$V_3 = V_2 + \frac{z_3^2}{2}.$$

The $(z_1, z_2, z_3) -$ susbsystem's trajectories are used to calculate the time derivative of V_3, which is provided by

$$\dot{V}_3 = \dot{V}_2 + z_2 \dot{z}_3.$$

An explicit calculation of $\dot{V}_3$ yields

$$\dot{V}_3 = -\mu z_1^2 - (\mu_1 + \gamma) z_2^2 - (\sigma + \mu) z_3^2 + z_3 \left[\gamma z_1 + \left(\beta x_4 + \frac{\gamma^2}{\sigma} \right) z_2 + \beta y_2 e_4 + \mu_2 \right].$$

If we choose $\mu_2 = -\gamma z_1 - \left(\beta x_4 + \frac{\gamma^2}{\sigma} \right) z_2 - \beta y_2 e_4$, then this implies that $\dot{V}_3 < 0$. From all the above, the states $(z_1, z_2, z_3) = (e_1, e_2, e_3 + \frac{\gamma}{\sigma} z_1)$ of the subsystem (5.11) converge to $(0, 0, 0)$.

Moreover, from the fourth equation of the system (5.8) and since e_2 converges to zero, then we deduce that the state e_4 converges asymptotically to zero.

Stated otherwise, the trajectories of the drive system represented by (5.5) and the controlled response system defined by (5.6) will asymptotically coincide with each other when the control input μ_2 is implemented. This result has a major impact in practice because our control law allows us to follow the behaviour of a SEIR model where the situation with the disease is not good to the behaviour of a SEIR model where the situation with the disease is good and controlled.

5.4.1. Experimental results for tracking

We consider the SEIR model with the following nomial parameters $\alpha = 0.07$, $\beta = 0.7$, $\mu = 0.05$, $\gamma = 0.07$, $\sigma = 0.02$ and $A = 0.08$. The initial conditions for the drive system (5.5) are $x_1(0) = 0.07$, $x_2(0) = 0.1$, $x_3(0) = 0.03$, $x_4(0) = 0.9$ and the response system (5.6) are $y_1(0) = 0.1$, $y_2(0) = 0.4$, $y_3(0) = 0.4$, $y_4(0) = 0.2$. Moreover, we have introduced the control input μ_2 to the response system at $t = 15$.

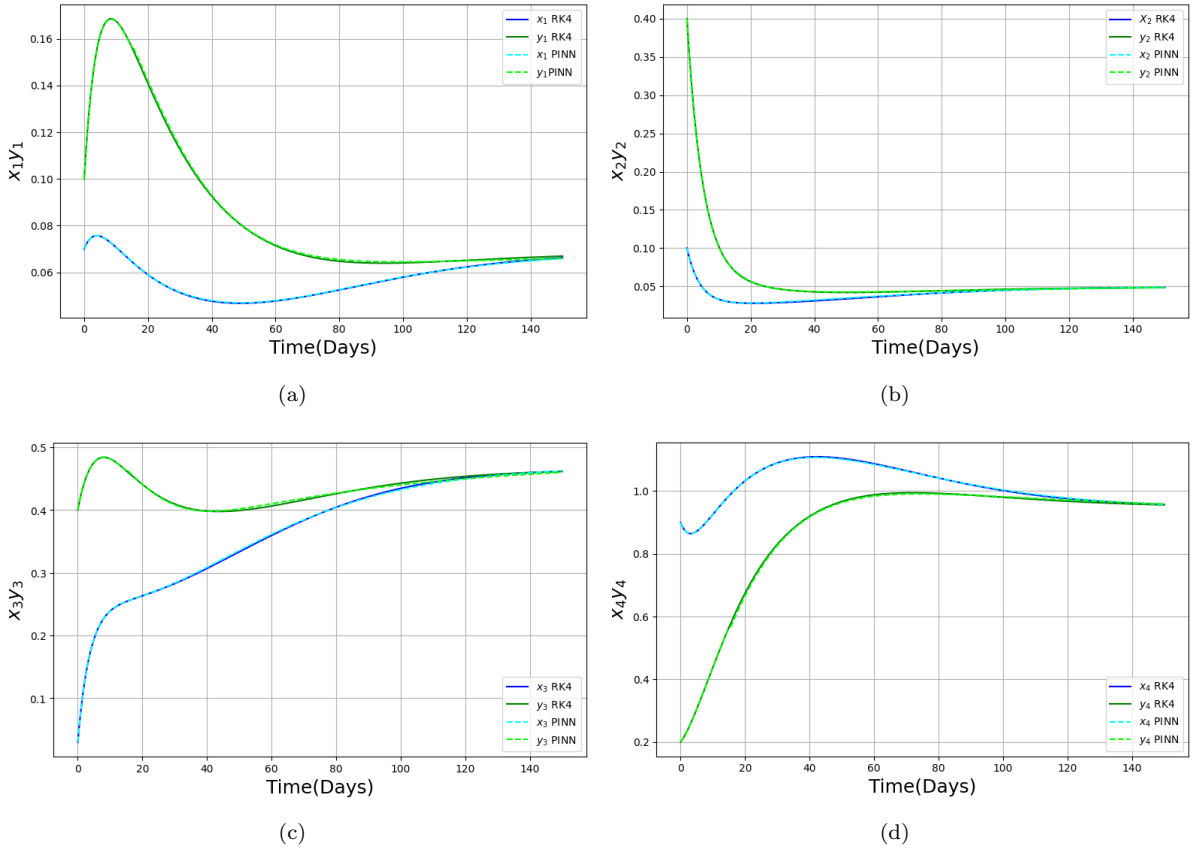

Figure 10. Comparison of results obtained using RK4 and PINNs.

Remark 5.6. Figure 10 illustrates the synchronization of the state variables x_1, x_2, x_3, x_4 of the drive system with the corresponding response system states y_1, y_2, y_3, y_4, as defined in equations (5.5) and (5.6). Biologically, synchronization implies that the dynamics of two interconnected or interacting systems such as different regions, populations, or control strate-

gies are aligned over time. This reflects coordinated epidemic behavior, which can be crucial when modeling the spread of disease across connected populations or implementing synchronized intervention strategies.

It is observed that the PINNs approach provides a significantly clearer and more detailed solution than the RK4 method, offering smoother trajectories and more precise convergence. This enhanced resolution allows for better analysis of the synchronization process and its biological implications. The results underscore the effectiveness of the PINNs framework in capturing complex dynamical interactions and producing more reliable solutions compared to traditional numerical methods.

6. Parameter identification using PINNs

In this section, we focus on parameter identification using our PINNs model. Let $p = (p_t, p_f)$ denote the set of parameters, where $p_t \in \mathbb{R}^{k_t}$ are the trainable parameters and $p_f \in \mathbb{R}^{k_f}$ are fixed, such that $k = k_t + k_f$. Additionally, let u^i_{data} represent the observed data at time points $t_1, \ldots, t_{N_{\text{data}}}$. Our goal is to solve the corresponding inverse problem

$$\arg\min_{p_t} L_{\text{data}}(\theta). \tag{6.1}$$

Now, in order to approximate the inverse problem (6.1), we release the parameters p_t in the minimization problem (4.8) and obtain

$$\arg\min_{\theta, p_t} \left(L_{\text{data}}(\theta) + L_{\mathcal{F}}(\theta)\right). \tag{6.2}$$

Therefore, we approximate the solution of the discrete inverse problem. Minimizing with respect to the trainable parameters p_t implies that, during the training phase of the PINN i.e., while optimizing the neural network, the parameters p_t are treated as variables. In this sense, p_t effectively becomes an additional trainable parameters of the network, similar to θ. This approach is justified, as the residual loss $L_{\mathcal{F}}(\theta)$ inherently depends on p_t. To enhance the optimization of (6.2), a weighting factor ω can be introduced to balance the different loss components, resulting in

$$\arg\min_{\theta, p_t} \left(L_{\text{data}}(\theta) + \omega L_{\mathcal{F}}(\theta)\right). \tag{6.3}$$

6.1. Application to SEIR models

In this section, we employ PINNs to approximate the inverse problem (6.1) for the SEIR model, utilizing temporal epidemiological data for the susceptible, exposed, infected, and recovered populations. The SEIR model is treated as a system of ODEs, which we reduce to the four main compartments: S, E, I, and R, as outlined in Section 2. Specifically, we focus on the formulation given in (2.1) for the SEIR dynamics. The corresponding PINN is constructed by training a neural network (4.5) on the available data using the composite loss function defined in (4.6).

Extending this framework to the SEIR model is straightforward. In particular, we consider the neural network

$$u_\theta(t_i) : \mathbb{R} \to \mathbb{R}^4,$$

$$t \mapsto \begin{pmatrix} \mathcal{S}_\theta \\ \mathcal{E}_\theta \\ \mathcal{I}_\theta \\ \mathcal{R}_\theta \end{pmatrix} =: \begin{pmatrix} \mathcal{S} \\ \mathcal{E} \\ \mathcal{I} \\ \mathcal{R} \end{pmatrix}$$

for approximating $(S(t), E(t), I(t), R(t))^T$ (see also (4.5) and Section 2). Then, we choose $p_t = \beta$ and $p_f = (A, \mu, \sigma, \alpha, \gamma)$ and again minimize the loss function

$$\arg\min_{\theta,\beta} \left(L_{\text{data}}(\theta) + \omega L_{\mathcal{F}}(\theta)\right),$$

where the residual is given by

$$\mathcal{F}(t, u, \frac{du}{dt}, \frac{d^2u}{dt^2}, ...) = \begin{pmatrix} \frac{\partial \mathcal{S}}{\partial t}(t) - A + \mu S(t) + \beta S(t) I(t) \\ \frac{\partial \mathcal{E}}{\partial t}(t) - \beta S(t) I(t) + (\sigma + \mu) E(t) \\ \frac{\partial \mathcal{I}}{\partial t}(t) - \sigma E(t) + (\alpha + \mu + \gamma) I(t) \\ \frac{\partial \mathcal{R}}{\partial t}(t) - \gamma I(t) + \mu R(t) \end{pmatrix}.$$

We remark that solving the inverse problem (4.8) is referred to as the data-driven discovery of differential equations in [14]. In this work, our goal is to utilize such data-driven discovery, i.e., parameter identification, along with PINNs to estimate the contact rate β of an SEIR model. Specifically, using PINNs for data-driven discovery and parameter estimation of ordinary differential equations means employing PINNs to solve an inverse problem. Unlike the more conventional approach of solving forward problems, where there is a distinct offline training phase followed by an online testing phase, we do not follow this typical structure. Instead, in the inverse problem context, we employ separate neural networks for each segment of the parameter β, each trained explicitly on the corresponding training data for the compartments S, E, I, and R.

It is important to note that, in contrast to [14], we propose a method that allows for the estimation of a time-dependent parameter β in (2.1). This represents a significant novelty compared to [14], where the data-driven discovery of partial differential equations is applied to estimate a model parameter that remains constant over time. Our approach involves partitioning the entire interval $[t_0, T]$ for parameter identification into smaller time intervals. Within each of these intervals, we assume that β is constant and compute an estimate using the machine learning approach described in this section. Notably, this method can easily be executed in parallel for all time intervals, allowing for quick updates whenever new data becomes available. Finally, we combine the individual estimates of β.

Remark 6.1. Let us briefly discuss the biological implications of selecting a specific value for the contact rate β. As observed, increasing the number of training epochs leads to a more pronounced smoothing effect on short-term fluctuations in β. This behavior arises from the assumption that β remains constant within each local time frame, allowing the model to better capture long-term trends while filtering out noise or minor irregularities. Biologically, β represents the rate at which susceptible individuals come into contact with infectious individuals and become

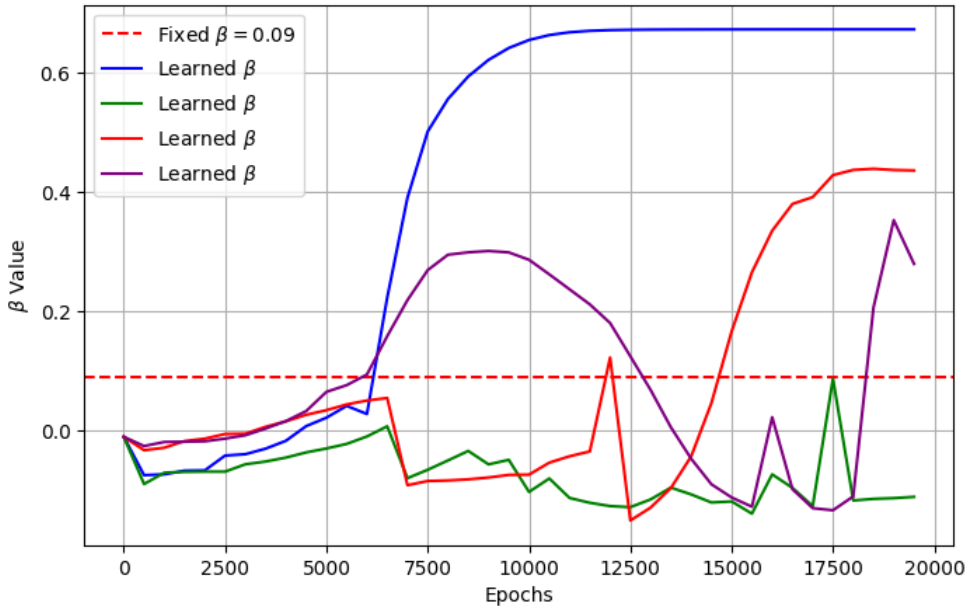

Figure 11. Estimates for β for an SEIR model for a contact rate with a sharp jump. We show comparative results for different initial conditions.

exposed. Therefore, accurately modeling its temporal behavior is essential for understanding the spread and control of an infectious disease. An underestimated or overestimated β could lead to incorrect predictions about the speed and extent of disease transmission. Figure 11 clearly demonstrates how the choice of β influences the model output, highlighting the importance of selecting an appropriate value that reflects realistic contact dynamics within the population. It is also observed that the optimal estimated value of β is typically obtained within 5000 to 7000 epochs.

7. Discussion and conclusion

This study successfully demonstrates the implementation of Physics-Informed Neural Networks (PINNs) to simulate the dynamics of disease spread within the Susceptible-Exposed-Infectious-Recovered (SEIR) model. By leveraging a fully connected neural network in PyTorch and utilizing automatic differentiation, we effectively enforced initial conditions and solved the system of ordinary differential equations (ODEs) governing the model. The custom loss function, which integrates boundary conditions with physics-informed terms, allowed for accurate modeling of the temporal progression of each compartment within the SEIR framework. Our findings underscore the historical significance of mathematical models in epidemiology, particularly the SEIR model's capacity to capture the complexities of disease transmission dynamics. By applying the PINNs approach, we explored the local and global stability of the SEIR model at both disease-free and endemic equilibrium points, while also assessing conditions for solution positivity and boundedness.

Notably, our research extends previous work by confirming the global stability of the complete SEIR system, numerically, without relying on the assumption of a constant population size, employing a generalized Lyapunov theorem for our analysis. The incorporation of physical constraints into the learning process not only contributes to the control and stabilization of the

SEIR model but also offers a pathway for developing effective control laws to eliminate infection persistence. Beyond forward simulation, this work addresses the inverse problem of parameter estimation specifically, identifying the time-dependent contact rate using temporal epidemiological data. By training the network on observed data for the susceptible, exposed, infectious, and recovered populations, the model approximates the solution vector and simultaneously minimizes a loss that combines data fidelity with the residual of the SEIR system.

The significance of this work extends to medical and public health applications, particularly in improving real-time epidemic forecasting and informing intervention strategies. By integrating data-driven methods with epidemiological models, PINNs provide a framework for more accurate and computationally efficient disease spread predictions, enabling healthcare professionals and policymakers to make informed decisions regarding containment measures, vaccination strategies, and resource allocation.

For future work, we aim to enhance the application of PINNs by integrating real-world epidemiological data to refine predictions and improve model generalization. We will explore the extension of PINNs to more complex epidemic models incorporating spatial dynamics, stochastic effects, and intervention measures such as vaccination and quarantine. Additionally, further validation will be conducted using graphical and statistical analyses to compare PINN-based solutions with traditional numerical methods, assessing error metrics and computational efficiency. These advancements will contribute to developing robust machine-learning-driven models for disease dynamics, ultimately benefiting medical research and public health planning.

The proposed PINN framework is effective for SEIR modeling and parameter estimation, but its accuracy depends on data quality and availability. It may require adaptation for more complex or different epidemic models. Additionally, training can be computationally intensive. Despite these limitations, the approach remains a flexible and powerful tool for real-time epidemiological analysis.

Funding. This research was funded by Basque Government, grant number [IT1555-22].

Acknowledgments. The authors would like to thank the Basque Government for supporting this research work through Grant IT1555-22. They also thank MICIU/AEI/10.13039/501100011033 and FEDER/UE for partially funding their research work through Grants PID2021-123543OB-C21 and PID2021-123543OB-C22.

Data availability. Not applicable.

Human and animal ethics. Not applicable.

Code. Codes can be obtained at https://github.com/shahbaz1982/SEIR.

References

[1] A. Abta, A. Kaddar and H. T. Alaoui, *Global stability for delay SIR and SEIR epidemic models with saturated incidence rates*, Electronic Journal of Differential Equations, 2012, 2012(23), 1–13.

[2] A. Abta, H. Laarabi and H. T. Alaoui, *The Hopf bifurcation analysis and optimal control of a delayed SIR epidemic model*, International Journal of Analysis, 2014, 2014(1), 940819.

[3] H. N. Agiza and M. T. Yassen, *Synchronization of Rossler and Chen chaotic dynamical systems using active control*, Physics Letters A, 2001, 278(4), 191–197.

[4] R. Anderson, *Infectious Diseases of Humans: Dynamics and Control*, Cambridge University Press, 1991.

[5] R. M. Anderson and R. M. May, *Population biology of infectious diseases: Part I*, Nature, 1979, 280, 361–367.

[6] H. Baty, *Solving stiff ordinary differential equations using physics informed neural networks (PINNs): Simple recipes to improve training of vanilla-PINNs*, arXiv preprint, 2023. arXiv:2304.08289.

[7] N. G. Bulgakov and B. S. Kalitin, *A generalization of theorems of Ljapunov's second method, I. Theory*, Vesci Akad. Navuk BSSR Ser. Fiz.-Mat. Navuk, 1978, 3(3), 32–36.

[8] A. I. K. Butt, W. Ahmad, H. G. Rabbani, M. Rafiq, S. Ahmad, N. Ahmad and S. Malik, *Exploring optimal control strategies in a nonlinear fractional bi-susceptible model for Covid-19 dynamics using Atangana-Baleanu derivative*, Scientific Reports, 2024, 14(1), 31617.

[9] X. Chen and S. Zhang, *An SEIR model for information propagation with a hot search effect in complex networks*, Mathematical Biosciences and Engineering, 2022, 20(1), 1251–1273.

[10] O. Diekmann and J. A. P. Heesterbeek, *Mathematical epidemiology of infectious diseases: Model building, analysis and interpretation*, John Wiley & Sons, 2000, 5.

[11] O. Diekmann, J. A. P. Heesterbeek and J. A. J. Metz, *On the definition and the computation of the basic reproduction ratio R_0 in models for infectious diseases in heterogeneous populations*, Journal of Mathematical Biology, 1990, 28, 365–382.

[12] K. Dietz and J. A. P. Heesterbeek, *Daniel Bernoulli's epidemiological model revisited*, Mathematical Biosciences, 2002, 180(1–2), 1–21.

[13] P. Van den Driessche and J. Watmough, *Reproduction numbers and sub-threshold endemic equilibria for compartmental models of disease transmission*, Mathematical Biosciences, 2002, 180(1–2), 29–48.

[14] V. Grimm, A. Heinlein, A. Klawonn, M. Lanser and J. Weber, *Estimating the time-dependent contact rate of SIR and SEIR models in mathematical epidemiology using physics-informed neural networks*, Electron. Trans. Numer. Anal., 2022, 56, 1–27.

[15] J. A. Haider, S. Ahmad, R. Alroobaea and I. E. Elseesy, *Applications of the Homotopy-based Fourier transform method for the dynamic solutions of differential equations*, Modern Physics Letters B, 2025, 39(12), 2450462.

[16] P. Hartman, *A lemma in the theory of structural stability of differential equations*, Proceedings of the American Mathematical Society, 1960, 11(4), 610–620.

[17] S. He, Y. Peng and K. Sun, *SEIR modeling of the COVID-19 and its dynamics*, Nonlinear Dynamics, 2020, 101(3), 1667–1680.

[18] J. M. Heffernan, R. J. Smith and L. M. Wahl, *Perspectives on the basic reproductive ratio*, Journal of the Royal Society Interface, 2005, 2(4), 281–293.

[19] H. W. Hethcote, *The mathematics of infectious diseases*, SIAM Review, 2000, 42(4), 599–653.

[20] M. J. Keeling and P. Rohani, *Modeling Infectious Diseases in Humans and Animals*, Princeton University Press, 2008.

[21] W. O. Kermack and A. G. McKendrick, *A contribution to the mathematical theory of epidemics*, Proceedings of the Royal Society of London, Series A, Containing Papers of a Mathematical and Physical Character, 1927, 115(772), 700–721.

[22] H. K. Khalil, *Nonlinear systems*, 2002, 3.

[23] P. V. Kokotović, I. Kanellakopoulos and A. S. Morse, *Adaptive feedback linearization of nonlinear systems*, Foundations of Adaptive Control, 2006, 309–346.

[24] A. Korobeinikov, *Lyapunov functions and global properties for SEIR and SEIS epidemic models*, Mathematical Medicine and Biology: A Journal of the IMA, 2004, 21(2), 75–83.

[25] A. Korobeinikov, *Lyapunov functions and global stability for SIR and SIRS epidemiological models with non-linear transmission*, Bulletin of Mathematical Biology, 2006, 68, 615–626.

[26] A. Korobeinikov, *Global properties of infectious disease models with nonlinear incidence*, Bulletin of Mathematical Biology, 2007, 69, 1871–1886.

[27] M. Krstić, I. Kanellakopoulos and P. V. Kokotović, *Nonlinear and adaptive control design*, (No Title), 1995.

[28] C. Li, X. Lü, J. Gong and Y. Lei, *Extended SEIR model of COVID-19 spread focusing on compartmental flow in England*, Nonlinear Dynamics, 2025, 113, 971–988.

[29] M. Y. Li and J. S. Muldowney, *Global stability for the SEIR model in epidemiology*, Mathematical Biosciences, 1995, 125(2), 155–164.

[30] M. Y. Li, H. L. Smith and L. Wang, *Global dynamics of an SEIR epidemic model with vertical transmission*, SIAM Journal on Applied Mathematics, 2001, 62(1), 58–69.

[31] T. Liao and S. Tsai, *Adaptive synchronization of chaotic systems and its application to secure communications*, Chaos, Solitons & Fractals, 2000, 11(9), 1387–1396.

[32] E. Madenci and I. Guven, *The Finite Element Method and Applications in Engineering Using ANSYS®*, Springer, 2015.

[33] A. Mannan, J. Ul Rahman, Q. Iqbal and R. Zulfiqar, *Design of periodic neural networks for computational investigations of nonlinear hepatitis C virus model under boozing*, Computation, 2025, 13(3), 66.

[34] A. Mannan, N. Shoket, J. Ul Rahman and R. Uwitije, *Dynamic analysis of ebola virus disease with non-linear incidence rate using morlet wavelet neural networks and hybrid optimization techniques*, Modeling Earth Systems and Environment, 2025, 11(2), 79.

[35] F. Mortaji, A. Abta, H. Laarabi and M. Rachik. *Global stability analysis, stabilization and synchronization of an SEIR epidemic model*, International Journal of Control, 2024, 1–15.

[36] N. Mustafa, J. Ul Rahman, U. Ishtiaq and I. Popa, *Artificial neural network-based approach for dynamic analysis and modeling of Marburg virus epidemics for health care*, Symmetry, 2025, 17(4), 578.

[37] N. Mustafa, J. Ul Rahman and A. Omame, *Modelling of Marburg virus transmission dynamics: A deep learning-driven approach with the effect of quarantine and health awareness interventions*, Modeling Earth Systems and Environment, 2024, 1–21.

[38] X. Ning, L. Jia, Y. Wei, X. Li and F. Chen, *Epi-DNNs: Epidemiological priors informed deep neural networks for modeling COVID-19 dynamics*, Computers in Biology and Medicine, 2023, 158, 106693.

[39] A. N. Njah and O. D. Sunday, *Synchronization of identical and non-identical 4-D chaotic systems via Lyapunov direct method*, International Journal of Nonlinear Science, 2009, 8(1), 3–10.

[40] M. Nuno, Z. Feng, M. Martcheva and C. Castillo-Chavez, *Dynamics of two-strain influenza with isolation and partial cross-immunity*, SIAM Journal on Applied Mathematics, 2005, 65(3), 964–982.

[41] J. Rahman, *DiffGrad for physics-informed neural networks*, arXiv preprint, 2024. arXiv:2409.03239.

[42] M. Raissi, P. Perdikaris and G. E. Karniadakis, *Physics-informed neural networks: A deep learning framework for solving forward and inverse problems involving nonlinear partial differential equations*, Journal of Computational Physics, 2019, 378, 686–707.

[43] A. Rasool, J. Ul Rahman and R. Uwitije, *Enhancing molecular property prediction with quantized GNN models*, Journal of Cheminformatics, 2025, 17(1), 1–19.

[44] M. De la Sen, R. P. Agarwal, A. Ibeas and S. Alonso-Quesada, *On a generalized time-varying SEIR epidemic model with mixed point and distributed time-varying delays and combined regular and impulsive vaccination controls*, Advances in Difference Equations, 2010, 2010, 1–42.

[45] M. De la Sen, R. P. Agarwal, A. Ibeas and S. Alonso-Quesada, *On the existence of equilibrium points, boundedness, oscillating behavior and positivity of a SVEIRS epidemic model under constant and impulsive vaccination*, Advances in Difference Equations, 2011, 2011, 1–32.

[46] J. Sirignano and K. Spiliopoulos, *DGM: A deep learning algorithm for solving partial differential equations*, Journal of Computational Physics, 2018, 375, 1339–1364.

[47] J. T. Spooner, M. Maggiore, R. Ordonez and K. M. Passino, *Stable adaptive control and estimation for nonlinear systems: Neural and fuzzy approximator techniques*, John Wiley & Sons, 2004.

[48] T. T. Tran, *Nonlinear Flight Control Design Using Backstepping Methodology*, Old Dominion University, 2016.

[49] B. Wang and G. Wen, *On the synchronization of a class of chaotic systems based on backstepping method*, Physics Letters A, 2007, 370(1), 35–39.

[50] W. Wang, J. Xin and F. Zhang, *Persistence of an SEIR model with immigration dependent on the prevalence of infection*, Discrete Dynamics in Nature and Society, 2010, 2010(1), 727168.

[51] Z. Wang, C. T. Bauch, S. Bhattacharyya, A. d'Onofrio, P. Manfredi, M. Perc, N. Perra, M. Salathé and D. Zhao, *Statistical physics of vaccination*, Physics Reports, 2016, 664, 1–113.

[52] E. Weinan, *The dawning of a new era in applied mathematics*, Notices of the American Mathematical Society, 2021, 68(4), 565–571.

[53] P. J. Witbooi, S. M. Vyambwera and M. U. Nsuami, *Control and elimination in an SEIR model for the disease dynamics of COVID-19 with vaccination*, AIMS Mathematics, 2023, 8(4), 8144–8161.

[54] Z. Yang, Z. Zeng, K. Wang, S. Wong, W. Liang, M. Zanin, P. Liu, X. Cao, Z. Gao and Z. Mai, *Modified SEIR and AI prediction of the epidemics trend of COVID-19 in China under public health interventions*, Journal of Thoracic Disease, 2020, 12(3), 165.

[55] M. T. Yassen. *Chaos control of chaotic dynamical systems using backstepping design*, Chaos, Solitons & Fractals, 2006, 27(2), 537–548.

[56] B. Yu. *The deep Ritz method: A deep learning-based numerical algorithm for solving variational problems*, Communications in Mathematics and Statistics, 2018, 6(1), 1–12.

[57] Z. Zhang, J. Wu, Y. Suo and X. Song. *The domain of attraction for the endemic equilibrium of an SIRS epidemic model*, Mathematics and Computers in Simulation, 2011, 81(9), 1697–1706.

Received May 2025; Accepted August 2025; Available online September 2025.